Research Article | Vol. 8, No. 10 | 1 Oct 2017 | BIOMEDICAL OPTICS EXPRESS 4331
Biomedical Optics EXPRESS

Imaging of neuronal tissues by x-ray diffraction and x-ray fluorescence microscopy: evaluation of contrast and biomarkers for neurodegenerative diseases

ELEONORA CARBONI,[1,2,5] JAN-DAVID NICOLAS,[3,5] MAREIKE TÖPPERWIEN,[2,3] CHRISTINE STADELMANN-NESSLER,[4] PAUL LINGOR,[1,2,6] AND TIM SALDITT[2,3,7]

[1]*Klinik für Neurologie, Universitätsmedizin Göttingen, Robert-Koch-Str. 40, 37075 Göttingen, Germany*
[2]*Cluster of Excellence "Nanoscale Microscopy and Molecular Physiology of the Brain", Humboldtallee 23, 37073 Göttingen, Germany*
[3]*Institut für Röntgenphysik, Friedrich-Hund-Platz 1, 37077 Göttingen, Germany*
[4]*Institut für Neuropathologie, Universitätsmedizin Göttingen, Robert-Koch-Str. 40, 37075 Göttingen, Germany*
[5]*These authors contributed equally*
[6]*plingor@gwdg.de*
[7]*tsaldit@gwdg.de*

Abstract: We have used scanning X-ray diffraction (XRD) and X-ray fluorescence (XRF) with micro-focused synchrotron radiation to study histological sections from human substantia nigra (SN). Both XRF and XRD mappings visualize tissue properties, which are inaccessible by conventional microscopy and histology. We propose to use these advanced tools to characterize neuronal tissue in neurodegeneration, in particular in Parkinson's disease (PD). To this end, we take advantage of the recent experimental progress in x-ray focusing, detection, and use automated data analysis scripts to enable quantitative analysis of large field of views. XRD signals are recorded and analyzed both in the regime of small-angle (SAXS) and wide-angle x-ray scattering (WAXS). The SAXS signal was analyzed in view of the local myelin structure, while WAXS was used to identify crystalline deposits. PD tissue scans exhibited increased amounts of crystallized cholesterol. The XRF analysis showed increased amounts of iron and decreased amounts of copper in the PD tissue compared to the control.

OCIS codes: (180.7460) X-ray Microscopy; (180.5810) Scanning microscopy; (170.6510) Spectroscopy, tissue diagnostics; (170.6935) Tissue characterization.

References and links

1. L. Bertram and R. E. Tanzi, "The genetic epidemiology of neurodegenerative disease," J. Clin. Invest. **115**, 1449–1457 (2005).
2. A. J. Hughes, S. E. Daniel, Y. Ben-Shlomo, and A. J. Lees, "The accuracy of diagnosis of parkinsonian syndromes in a specialist movement disorder service," Brain **125**, 861 (2002).
3. M. G. Spillantini, M. L. Schmidt, V. M.-Y. Lee, J. Q. Trojanowski, R. Jakes, and M. Goedert, "α-synuclein in lewy bodies," Nature **388**, 839–840 (1997).
4. D. T. Dexter, F. R. Wells, A. J. Lee, F. Agid, Y. Agid, P. Jenner, and C. D. Marsden, "Increased nigral iron content and alterations in other metal ions occurring in brain in parkinson's disease," J. Neurochem. **52**, 1830–1836 (1989).
5. M. Szczerbowska-Boruchowska, A. Krygowska-Wajs, and D. Adamek, "Elemental micro-imaging and quantification of human substantia nigra using synchrotron radiation based x-ray fluorescence - in relation to parkinson's disease," J. Phys. Condens. Matter **24**, 244104 (2012).
6. V. Dias, E. Junn, and M. M. Mouradian, "The role of oxidative stress in parkinson's disease," J. Parkinsons Dis. **3**, 461–491 (2013).
7. E. Carboni and P. Lingor, "Insights on the interaction of alpha-synuclein and metals in the pathophysiology of Parkinson's disease," Metallomics **7**, 395–404 (2015).
8. J. Meiser, D. Weindl, and K. Hiller, "Complexity of dopamine metabolism," Cell Commun. Signal **11**, 34 (2013).

#301637 https://doi.org/10.1364/BOE.8.004331
Journal © 2017 Received 4 Jul 2017; revised 10 Aug 2017; accepted 17 Aug 2017; published 5 Sep 2017

Biomedical Optics EXPRESS

9. D. Sulzer, J. Bogulavsky, K. E. Larsen, G. Behr, E. Karatekin, M. H. Kleinman, N. Turro, D. Krantz, R. H. Edwards, L. A. Greene, and L. Zecca, "Neuromelanin biosynthesis is driven by excess cytosolic catecholamines not accumulated by synaptic vesicles," Proc. Natl. Acad. Sci. **97**, 11869–11874 (2000).
10. F. A. Zucca, J. Segura-Aguilar, E. Ferrari, P. Muñoz, I. Paris, D. Sulzer, T. Sarna, L. Casella, and L. Zecca, "Interactions of iron, dopamine and neuromelanin pathways in brain aging and parkinson's disease," Prog. Neurobiol. **155**, 96–119 (2017).
11. M. Doria, L. Maugest, T. Moreau, G. Lizard, and A. Vejux, "Contribution of cholesterol and oxysterols to the pathophysiology of parkinson's disease," Free Radic. Biol. Med. **101**, 393–400 (2016).
12. A. Sakdinawat and D. Attwood, "Nanoscale x-ray imaging," Nat. Photon. **4**, 840–848 (2010).
13. J. Stangl, C. Mocuta, V. Chamard, and D. Carbone, *Nanobeam X-ray Scattering: Probing Matter at the Nanoscale* (WILEY-VCH Verlag GmbH & Co. KGaA, 2014).
14. S. Vogt, J. Maser, and C. Jacobsen, "Data analysis for x-ray fluorescence imaging," J. Phys. IV France **104**, 617–622 (2003).
15. C. J. Fahrni, "Biological applications of x-ray fluorescence microscopy: exploring the subcellular topography and speciation of transition metals," Curr. Opin. Chem. Biol. **11**, 121–127 (2007).
16. T. Salditt and T. Dučić, *Super-Resolution Microscopy Techniques in the Neurosciences* (Humana Press, Totowa, NJ, 2014), Chap. X-Ray Microscopy for Neuroscience: Novel Opportunities by Coherent Optics, pp. 257–290.
17. S. Bohic, K. Murphy, W. Paulus, P. Cloetens, M. Salomé, J. Susini, and K. Double, "Intracellular chemical imaging of the developmental phases of human neuromelanin using synchrotron x-ray microspectroscopy," Anal. Chem. **80**, 9557–9566 (2008).
18. M. Szczerbowska-Boruchowska, "X-ray fluorescence spectrometry, an analytical tool in neurochemical research," X-Ray Spectrom. **37**, 21–31 (2008).
19. T. Dučić, S. Quintes, K.-A. Nave, J. Susini, M. Rak, R. Tucoulou, M. Alevra, P. Guttmann, and T. Salditt, "Structure and composition of myelinated axons: A multimodal synchrotron spectro-microscopy study," J. Struct. Biol. **173**, 202–212 (2011).
20. S. A. James, D. E. Myers, M. D. de Jonge, S. Vogt, C. G. Ryan, B. A. Sexton, P. Hoobin, D. Paterson, D. L. Howard, S. C. Mayo, M. Altissimo, G. F. Moorhead, and S. W. Wilkins, "Quantitative comparison of preparation methodologies for x-ray fluorescence microscopy of brain tissue," Anal Bioanal Chem **401**, 853–864 (2011).
21. S. C. Dodani, D. W. Domaille, C. I. Nam, E. W. Miller, L. A. Finney, S. Vogt, and C. J. Chang, "Calcium-dependent copper redistributions in neuronal cells revealed by a fluorescent copper sensor and x-ray fluorescence microscopy," Proc. Natl. Acad. Sci. **108**, 5980–5985 (2011).
22. T. Jensen, M. Bech, O. Bunk, A. Menzel, A. Bouchet, G. L. Duc, R. Feidenhans'l, and F. Pfeiffer, "Molecular x-ray computed tomography of myelin in a rat brain," NeuroImage **57**, 124 – 129 (2011).
23. H. Lichtenegger, M. Müller, O. Paris, C. Riekel, and P. Fratzl, "Imaging of the helical arrangement of cellulose fibrils in wood by synchrotron X-ray microdiffraction," J. Appl. Crystallogr. **32**, 1127–1133 (1999).
24. P. Fratzl and R. Weinkamer, "Nature's hierarchical materials," Prog Mater Sci **52**, 1263–1334 (2007).
25. C. Riekel, M. Burghammer, T. G. Dane, C. Ferrero, and M. Rosenthal, "Nanoscale structural features in major ampullate spider silk," Biomacromolecules **18**, 231–241 (2017).
26. M. J. Lynch, S. S. Raphael, L. D. Mellor, P. D. Spare, and M. J. Inwood, *Medical Laboratory Technology and Clinical Pathology* (WB Saunders Co., 1969), 2nd ed.
27. A. H. Fischer, K. A. Jacobson, J. Rose, and R. Zeller, "Fixation and permeabilization of cells and tissues," Cold Spring Harb Protoc **2008**, 1–2 (2008).
28. V. Solé, E. Papillon, M. Cotte, P. Walter, and J. Susini, "A multiplatform code for the analysis of energy-dispersive x-ray fluorescence spectra," Spectrochim Acta B **62**, 63–68 (2007).
29. D. A. Kirschner and C. J. Hollingshead, "Processing for electron microscopy alters membrane structure and packing in myelin," J. Ultrastruct. Res. **73**, 211–232 (1980).
30. M. Bernhardt, J.-D. Nicolas, M. Eckermann, B. Eltzner, F. Rehfeldt, and T. Salditt, "Anisotropic x-ray scattering and orientation fields in cardiac tissue cells," New J. Phys. **19**, 013012 (2017).
31. R. Shaharabani, M. Ram-On, R. Avinery, R. Aharoni, R. Arnon, Y. Talmon, and R. Beck, "Structural transition in myelin membrane as initiator of multiple sclerosis," J. Am. Chem. Soc. **138**, 12159–12165 (2016).
32. R. T. Joy and J. B. Finean, "A comparison of the effects of freezing and of treatment with hypertonic solutions on the structure of nerve myelin," J. Ultrastruct. Res. **8**, 264–282 (1963).
33. J. Elkes and J. B. Finean, "X-ray diffraction studies on the effect of temperature on the structure of myelin in the sciatic nerve of the frog," Exp. Cell Res. **4**, 69–81 (1953).
34. J. B. Finean, "The nature and stability of nerve myelin," Int. Rev. Cytol. **12**, 303–336 (1962).
35. C. R. Worthington and A. R. Worthington, "Effect of heat on frog sciatic nerve determined by x-ray diffraction," Int. J. Biol. Macromol. **3**, 159–164 (1981).
36. J. N. Israelachvili, *Intermolecular and Surface Forces* (Academic Press, 2015).
37. H. S. Shieh, L. G. Hoard, and C. E. Nordman, "Crystal structure of anhydrous cholesterol," Nature **267**, 287–289 (1977).
38. K. M. Davies, S. Bohic, A. Carmona, R. Ortega, V. Cottam, D. J. Hare, J. P. M. Finberg, S. Reyes, G. M. Halliday, J. F. B. Mercer, and K. L. Double, "Copper pathology in vulnerable brain regions in parkinson's disease," Neurobiol Aging **35**, 858–866 (2014).

Biomedical Optics EXPRESS

39. A. Surowka, M. Töpperwien, M. Bernhardt, J. Nicolas, M. Osterhoff, T. Salditt, D. Adamek, and M. Szczerbowska-Boruchowska, "Combined in-situ imaging of structural organization and elemental composition of substantia nigra neurons in the elderly," Talanta **161**, 368–376 (2016).
40. L. Zecca, T. Shima, A. Stroppolo, C. Goj, G. Battiston, R. Gerbasi, T. Sarna, and H. Swartz, "Interaction of neuromelanin and iron in substantia nigra and other areas of human brain," Neuroscience **73**, 407–415 (1996).
41. M. Szczerbowska-Boruchowska, M. Lankosz, J. Ostachowicz, D. Adamek, A. Krygowska-Wajs, B. Tomik, A. Szczudlik, A. Simionovici, and S. Bohic, "Topographic and quantitative microanalysis of human central nervous system tissue using synchrotron radiation," X-Ray Spectrom **33**, 3–11 (2004).
42. A. Binolfi, R. M. Rasia, C. W. Bertoncini, M. Ceolin, M. Zweckstetter, C. Griesinger, T. M. Jovin, and C. O. Fernández, "Interaction of α-synuclein with divalent metal ions reveals key differences: a link between structure, binding specificity and fibrillation enhancement," J. Am. Chem. Soc. **128**, 9893–9901 (2006).
43. S. R. Paik, H.-J. Shin, J.-H. Lee, C.-S. Chang, and J. Kim, "Copper(ii)-induced self-oligomerization of α-synuclein," Biochem. J. **340**, 821–828 (1999).
44. V. N. Uversky, J. Li, and A. L. Fink, "Metal-triggered structural transformations, aggregation, and fibrillation of human α-synuclein: A possible molecular link between parkinson's disease and heavy metal exposure," J. Biol. Chem. **276**, 44284–44296 (2001).
45. J. Liu, I. Costantino, N. Venugopalan, R. F. Fischetti, B. T. Hyman, M. P. Frosch, T. Gomez-Isla, and L. Makowski, "Amyloid structure exhibits polymorphism on multiple length scales in human brain tissue," Sci. Rep. **6**, 33079 (2016).
46. C. R. Loomis, G. G. Shipley, and D. M. Small, "The phase behavior of hydrated cholesterol." J. Lipid Res. **20**, 525–535 (1979).
47. D. Cheng, A. M. Jenner, G. Shui, W. F. Cheong, T. W. Mitchell, J. R. Nealon, W. S. Kim, H. McCann, M. R. Wenk, G. M. Halliday, and B. Garner, "Lipid pathway alterations in parkinson's disease primary visual cortex," PLoS One **6**, 1–18 (2011).
48. Z. Li, J. Zhang, and H. Sun, "Increased plasma levels of phospholipid in parkinson's disease with mild cognitive impairment," J. Clin. Neurosci. **22**, 1268–1271 (2015).
49. A. Zarrouk, A. Vejux, J. Mackrill, Y. O'Callaghan, M. Hammami, N. O'Brien, and G. Lizard, "Involvement of oxysterols in age-related diseases and ageing processes," Ageing Res. Rev. **18**, 148–162 (2014).
50. M. Bousquet, I. St-Amour, M. Vandal, P. Julien, F. Cicchetti, and F. Calon, "High-fat diet exacerbates MPTP-induced dopaminergic degeneration in mice," Neurobiol. Dis. **45**, 529–538 (2012).
51. A. van Maarschalkerweerd, V. Vetri, and B. Vestergaard, "Cholesterol facilitates interactions between α-synuclein oligomers and charge-neutral membranes," FEBS Lett. **589**, 2661–2667 (2015).

1. Introduction

Parkinson's disease (PD) is the most common motor neurodegenerative disease worldwide and its prevalence is expected to dramatically increase in the near future because of the aging of the population [1]. The classical disease symptoms comprise (but are not limited to) motor symptoms such as rigidity, akinesia, rest tremor, and gait disturbance together with non-motor symptoms such as sleep disturbances, hyposmia and psychiatric symptoms. Despite intense research, PD diagnosis is still mostly relying on patients' symptoms and early biomarkers for the disease are still missing. In fact, only post-mortem analysis can ascertain PD diagnosis and exclude the presence of pathologies with similar symptomatology [2].

Histologically, PD brains show two well-known hallmarks: the depletion of dopaminergic neurons in the substantia nigra (SN) and the presence of protein aggregates named Lewy Bodies (LB) that are mainly formed by a protein called alpha-synuclein (aSyn) [3]. In addition to that, also iron (Fe) is thought to play an important role in PD pathophysiology as Fe dyshomeostasis in the patients' brains is well documented [4]. Specifically, in PD there is an accumulation of Fe in the SN of the patients [5]. This is of great interest, since this particular brain region is one of the most affected by the disease. Similarly to other neurodegenerative diseases, PD patients display increased levels of oxidative stress and reactive oxygen species (ROS) [6]. Several cellular processes are responsible for ROS increase and, in PD, Fe accumulation is definitely one of the most prominent reasons. In fact, Fe and other metals can actively participate in the so-called Fenton and Haber-Weiss reactions leading to the formation of the highly reactive hydroxyl radicals thus exacerbating oxidative stress [7]. Together with Fe also dopamine is involved in the increase of oxidative stress. In PD, dopaminergic neurons are affected in the course of the disease leading to the appearance of motor symptoms. Dopamine metabolism is implicated in

Biomedical Optics EXPRESS

the generation of ROS [8]. Among dopamine byproducts, neuromelanin (NM) is noteworthy [9]. In contrast to other dopamine metabolites, NM is thought to exert a protective role against oxidative stress [10]. Histologically, NM is a dark-brown pigment inside dopaminergic neurons of SN (hence the name of this region). Therefore, due to its color, NM can be used in unstained sections of SN to localize the dopaminergic neurons. Oxidative stress leads to the production of unbalanced free radicals that are able to oxidize proteins, DNA and lipids in the cell. Among oxidized lipids in PD, cholesterol and its oxidized byproducts (oxysterols) have shown to be involved in the exacerbation of the disease and might represent a possible biomarker for PD [11].

In this work, we explored whether scanning hard x-ray microscopy using focused synchrotron radiation can provide novel imaging modalities and 'structural biomarkers' in the context of PD research. To this end, we wanted to complement established histology of PD tissues by novel molecular contrast mechanisms and by two-dimensional (2D) mappings of these signals, yielding the micro-resolved spatial distribution of transition metals as well as the distribution of those molecular structures, which can be identified from their diffraction patterns. This is a timely effort, since significant progress in hard x-ray optics [12, 13] has now made possible to rapidly scan tissue sections with micro- or nanometer focal spot sizes. By automated analysis, 2D maps of x-ray fluorescence (XRF) and diffraction signals can then be generated, providing advanced contrast mechanisms of scanning transmission x-ray microscopy (STXM). STXM with XRF contrast [14] has already become a fairly well established method for trace element mapping in neural cells and tissues, as reviewed in [15] and in [16]. In contrast to electron microscopy based x-ray microanalysis (EDX), XRF collects signal from the interior of the tissue section, with a sensitivity down to a few hundred atoms of an element in a pixel, and can also be used for speciation. In particular, the elemental distribution of Fe, Cu, Zn, and Mn, with suspected roles in redox regulation or signaling, have been addressed [17–20]. In this context, the local spatial distribution is important. For example, it was shown by XRF mapping that neural cells redistribute significant pools of copper from their cell bodies to the periphery upon calcium activation [21]. Contrarily, scanning small-angle x-ray scattering (SAXS) and wide-angle x-ray scattering (WAXS) are largely unexplored for neural tissues, except for studies of myelin diffraction, see for example [19, 22]. These techniques have contributed to the understanding of biomaterials by local structure analysis [23–25]. This makes us confident that with further decrease of detection levels, scanning SAXS and WAXS can also be advantageously applied to soft biological tissues, in particular taking advantage of the recent experimental progress (e.g. focusing, detection, background suppression).

2. Materials and methods

Ethics Statement: All samples were obtained from the UK Brain Bank (Parkinson's UK, London, England) and approved by the Multicenter Research Ethics Committee (07/MRE09/72).

Demographics: PD sample (#ID: PD102). Age: 81, Braak stage: 6, disease duration: 25 years, post-mortem interval: 16 h. CTR sample (#ID: MS523). Age: 63, Braak stage: N/A, disease duration: N/A, post-mortem interval: 21 h.

Sample preparation: 30 µm thick tissue sections from snap frozen tissue blocks from the midbrain of one PD patient and one non-PD control patient were cut in a cryostat (CM3050 S, Leica, Nussloch, Germany) using special teflon-coated blades (DB80 LX, Nussloch, Germany) to avoid iron particles contamination due to the friction. During cutting, the sample temperature was kept at −17°C given a sample holder temperature of −15°C. After cutting, the sections were deposited onto SiN membranes ($8 \times 8\,\mathrm{mm}^2$ window size, 200 nm thickness, Silson Ltd., Southam, England) or onto 0.5 − 1 µm thick, stretched polypropylene foils. The samples were then air dried for 15 min at room temperature (RT) and dried for 30 min at 60°C. Finally, the samples were enclosed with a second SiN or polypropylene foil and sealed with nail polish.

X-ray fluorescence and scanning diffraction experiments: The samples were imaged at the

Biomedical Optics EXPRESS

ID13 beamline of the European Synchrotron Radiation Facility (Grenoble, France). A scheme of the experimental setup can be found in Fig. 1. The samples were mounted on a motorized stage

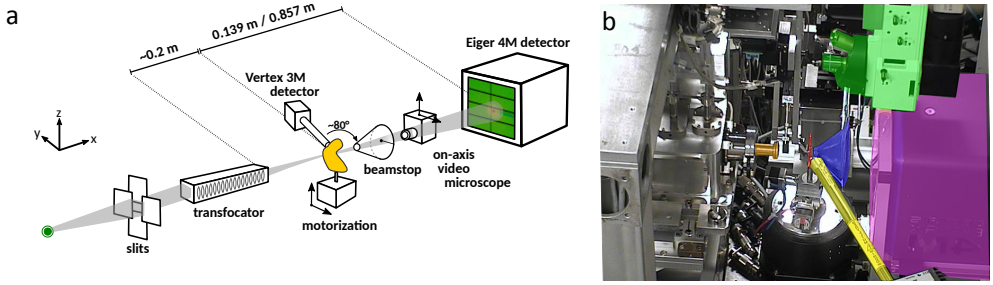

Fig. 1. Sketch of the experimental endstation. (a) Monochromatized undulator radiation is focused down to a spot size of $2 \times 3\,\mu m^2$ through a transfocator. The sample (tissue section on solid support, SiN window or polypropylene foil) is placed into the focus of the x-ray beam. Scattered radiation and fluorescence is detected simultaneously on a 2D pixelated detector (Eiger 4M, Dectris) and Vortex EM detector, respectively. An on-axis video microscope facilitates sample positioning and alignment. A circular beamstop blocks unscattered radiation at approx. 10 cm downstream of the focus position. A photograph of the setup is shown in (b). Individual components are highlighted in color: Transfocator exit window (orange), sample holder (red), Vortex EM detector (yellow), He-flushed flighttube (blue), on-axis microscope (green), and Eiger 4M detector (magenta).

and regions of interest were identified with a movable in-line optical microscope. Diffraction patterns were recorded using an Eiger 4M detector (Dectris, Baden-Daettwil, Switzerland) placed either 0.139 m or 0.857 m behind the sample to collect data in the wide and small angle range, respectively. Simultaneously, a Vortex EM detector (Hitachi High-Technologies Science America, Northridge, USA) was positioned in the horizontal plane and tilted at 80° with respect to the primary beam to record an X-ray fluorescence spectrum at each scan point. The distance of the detector entry window to the sample was 35 mm and 38 mm, for the SiN mounted tissues and polypropylene mounted tissues, respectively. The energy was set to 12.8 keV defined by the gap of the Si(111) channel-cut monochromator. Beam-defining slits and a transfocator were tuned to produce an elliptical spot of $2(h) \times 3(v)\,\mu m^2$. The step size in all scans was therefore set to 3 µm to avoid overlap of subsequent scan points. Typically, an acquisition time of 50 ms was chosen given an overall photon flux of 4.45×10^{11} photons/s.

Immunohistochemisty (IHC) of tissue sections: All chemicals were purchased by Sigma-Aldrich unless otherwise stated. After the synchrotron analyses the tissue blocks were fixated in 4% PFA (Roth, #0335) for 48h and subsequently embedded in paraffin. Histological evaluations were carried out on 4 µm thick sections after deparaffinization [26]. Briefly, the sections were submerged two times for 10 min in xylene and rehydrated in ethanol solutions of decreasing concentration for 5 min each step: 100%, 99%, 96%, 90%, 70% and 50% ethanol. For each sample, a section was stained with hematoxylin and eosin (HE) according to Mayer's method [27]. Briefly, the sections were put in hematoxylin solution (#H9627) for 10 min, then washed in water, and differentiated in 1% HCl-ethanol solution. Then, the slides were left 10 min to bluing in running tap water and finally rinsed in distilled water. The slides were incubated 3 min in eosin solution made with 0.25% eosin Y (#230251), 0.025% acetic acid (Roth, #6755) in 80% ethanol. Subsequently, the slides were washed in distilled water and dehydrated through passages in alcohol with ascending concentration of 70%, 90%, 95%, 99% and two times 100% for 3 min, lastly twice in xylene for 5 min. Slides were mounted with mounting medium (#06522).

The sections stained for alpha-synuclein (aSyn) and p129-aSyn underwent antigen retrieval in citrate buffer made with 10 mM sodium citrate (#251275), 0.05% TWEEN 20 (#P9416) at

Biomedical Optics EXPRESS

pH 6.0 for 3 times 5 min in the microwave. After cooling down, the slides for aSyn and myelin were only rinsed in distilled water and the endogenous peroxidases were inactivated in 3% H_2O_2 solution (Applichem, #121076) in phosphate-buffered saline (PBS) (Applichem, #A0964) for 10 min. After three washes in PBS, all the slides were blocked for 1 h in 10% fetal calf serum (FCS)/PBS (Biochrom, #S0615). The sections were incubated at 4°C overnight with the following antibodies: anti-human myelin basic protein (Dako, #A0623) dilution 1:2000; anti-human aSyn (Covance, SIG-39725) dilution 1:500, anti-p129-aSyn (Abcam, #PS129). After removal of the primary antibody, the secondary biotinylated antibodies were either sheep anti-mouse (Amersham, #RPN1001) or donkey anti-mouse (Amersham, #RPN1003) and were diluted in 1:200 and employed at RT for 45 min for the slides for aSyn and myelin. The revelation was achieved by diluting 1:1000 the avidin-peroxidase (#A3151) and leaving it in incubation for 45 min. After three rinses in PBS, slides were incubated in 1% DAB liquid substrate (#D7304) in PBS with the addition of 0.01% H_2O_2. For p129-aSyn stain, secondary antibody goat anti-rabbit conjugated with alkaline-phosphatase was used (Dako, #D0477) at RT for 45 min. For p129-aSyn a commercial kit was used for developing (DCS, #HK183-5K). After developing, all the slides were washed in PBS and counterstained with eosin, dehydrated and mounted as previously described.

3. Results

X-ray fluorescence results: XRF data was recorded from SN tissue sections with a total scanned area of 6.45 mm^2, divided into 2.52 mm^2 for the CTR and 3.93 mm^2 for the PD sample. From the scanned area, 5.83 mm^2 was used for a quantification of the elemental content of SN neurons. Maps of the distribution of single elements were obtained by a simple summation of the fluorescence intensity between the respective channel numbers after calibration of the detector. It was found that the Zn Kα line showed the most pronounced difference in signal originating from regions identified as intra-cellular and background regions. Using the Zn signal as a cell defining threshold, we have identified Zn thresholds in each scan for cell identification, as e.g. shown in Fig. 2 together with an optical micrograph for comparison. From the optical micrograph in Fig. 2(a), dopaminergic neurons are easily discernible because of the presence of the dark pigment NM. Therefore, even without staining, NM positive cells can be identified under an optical microscope. Figure 2 shows that there is a high correlation between the NM positive cells and the area identified by applying a simple threshold to the Zn Kα map (red contours in Fig. 2(b)).

For all scans, it was possible to separate areas of cellular signal and background. Hence, the summed spectra inside and outside of cells were generated for the PD and CTR samples respectively, and divided by the scanned area, resulting in four spectra which are shown in Fig. 3(a). Counts were normalized to the maximum intensity given by the elastic scattering peak. Once again, one can observe that the peak of Zn Kα fluorescence at 8.6 keV is higher for the cells and lower for the background, thus being consistent with our initial assumption. Elemental decomposition of the summed spectrum was carried out using the analysis software pyMCA [28]. Figure 3(b-e) depicts the results separately for intra- and extracellular, as well as for the PD and CTR sample. The presence of Si in the spectrum is due to the use of a Si-drift detector, while Ar is a major constituent of air. Contributions of P, S, and Cl at the lower end of the spectrum are too weak for a quantification, and will not be treated here. From the fitted spectrum, for each elemental component we have determined the variation in the relative concentration by subtracting the area under the elemental distribution from the PD sample from the CTR sample and divided by the area of the PD sample for normalization. Hence, formally, we can write (PD-CTR)/PD. This means that positive values refer to a higher concentration of an element in the PD sample relative to the CTR. All major components are summarized in this fashion in Fig. 3(f) along with their respective percentage variation with respect to the control sample.

Biomedical Optics EXPRESS

In the PD sample compared to the CTR, Fe amounts show a clear increase. Relative amounts are, in fact, 90 ± 12% in the intracellular space, while there is an increase of 277 ± 41% for the same element in the extracellular space. Regarding Cu, there is reduction in the PD sample compared to CTR. The intracellular relative amount of Cu is −68 ± 9%, while it is −55 ± 13% in the extracellular space.

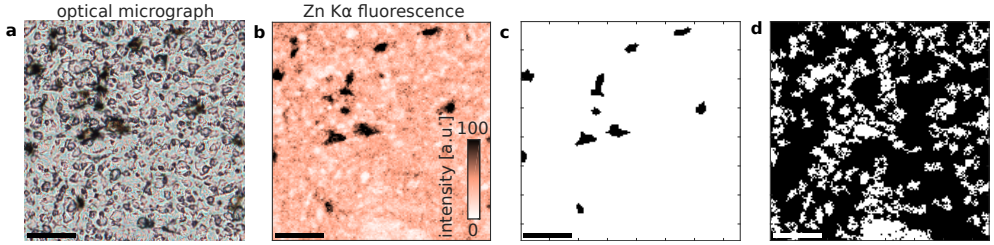

Fig. 2. (a) Optical micrograph corresponding to a region of a single scan on SN of PD sample. (b) Corresponding Zn Kα fluorescence intensity. Dark regions correspond to NM positive cells in the tissue. (c) Defining a fixed threshold of the Zn Kα fluorescence yields a logical map to locate the neuromelanin-positive cells (black). (d) A lower threshold yields a logical map corresponding to the extracellular region (black). Scale bar: 100 µm.

X-ray diffraction results: In addition to the element specific contrast, structural features were analyzed by means of x-ray diffraction. Scattering patterns were collected on a single photon counting 2D pixelated detector (Eiger 4M, 1 pixel point-spread function, Dectris, Switzerland) placed 0.139 m or 0.895 m downstream of the focus to collect the diffraction signal in the wide- and small angle range, respectively. With both detector positions, we could accommodate q_r ranges between 0.025 nm^{-1} to 4.1 nm^{-1}, suitable to detect reflections resulting from larger ultrastructures such as fibers, fibrils and lipid bilayer stacks as well as reflections from crystalline aggregations.

First, we analyzed the small-angle scattering signal that we tentatively attribute to the myelin sheath which surrounds the axon of nerve cells and facilitates nerve signal conduction. Myelin is an abundant component of neuronal tissue, however, its concentration varies based on the density of axons and degree of myelination in different brain regions. From the histological staining of myelin basic protein (MPB) shown in Fig. 4, it can be seen that the amount of myelin is reduced in the SN due to the high density of cell bodies of dopaminergic neurons that constitute the SN (Fig. 4(c)). On the other hand, the Red Nucleus (Fig. 4(d)) and the Crus Cerebri (CC, caudal region to the SN) (Fig. 4(b)) are richer in axons and thereby myelin, hence they appear darker in the stain.

Based on the hypothesis that the SAXS signal results from the myelin sheath, this difference in density of axons should translate into a higher scattered intensity of the SAXS signal from the CC. In Fig. 5(a-d) we show two darkfield maps from SN and fiber tract (FT) tissue from the CC. Data resulting from a homogeneous region in (a) and (c), marked roi 1 and roi 2, respectively, have been averaged and azimuthally integrated, as shown in (b) and (c). Two structure factor peaks are observed in both cases. Importantly, and supporting the myelin hypothesis, the reflection intensity recorded in the FT is stronger, by a factor of at least two. Further, the ratio of the two reflections is found to be 3/2. It is therefore plausible, that the inner and outer peak indicate a second and third order of a structure with a period of approximately 12.8 nm. In turn, this corresponds well to periods reported for myelin nerves that have been dried to prepare the sample for electron microscopy [29]. The observed peak positions and peak widths are summarized in Tab. 1. In addition, one should expect a more oriented alignment of the myelin signal in a region rich in neuronal connections due to the directed nature of neuronal connections linking different parts of the brain. To confirm this, we have quantified the level of anisotropy of the myelin

Biomedical Optics EXPRESS

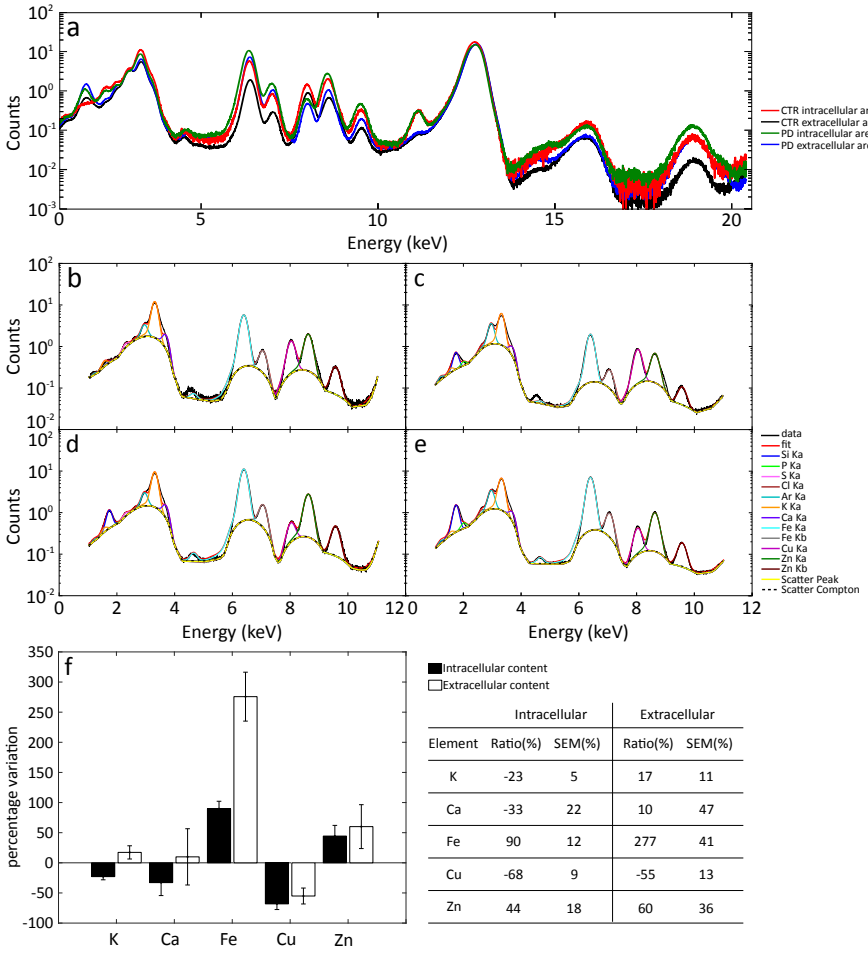

Element	Intracellular Ratio(%)	Intracellular SEM(%)	Extracellular Ratio(%)	Extracellular SEM(%)
K	-23	5	17	11
Ca	-33	22	10	47
Fe	90	12	277	41
Cu	-68	9	-55	13
Zn	44	18	60	36

Fig. 3. (a) Comparison of the averaged fluorescence spectra obtained from the cellular and extracellular regions of the PD and CTR sample. Note, that cells of the PD sample contain a higher amount of Fe with respect to the CTR. (b-e). Spectral decomposition of the data shown in A was done using pyMCA. (b) Spectral decomposition of the intracellular area of CTR. (c) Spectral decomposition of the extracellular area of CTR. (d) Spectral decomposition of the intracellular area of PD. (e) Spectral decomposition of the extracellular area of PD. Meaningful elements were selected for further quantification. (f) Ratios of fitted areas of the elements between PD and CTR. There is a higher concentration of Fe for the PD samples especially in the extracellular area, while the Cu concentration is reduced both in the extra- and intracellular compartment.

diffraction signal by performing a principal component analysis of the diffraction patterns, as previously introduced in [30]. In this approach, the covariance matrix of the distribution of the wavevector components q_y and q_z in the detection plane, defined as

$$C = \begin{pmatrix} \mathrm{var}(q_y) & \mathrm{cov}(q_y, q_z) \\ \mathrm{cov}(q_z, q_y) & \mathrm{var}(q_z) \end{pmatrix}$$

is diagonalized. The two corresponding eigenvectors $\vec{v}_1$ and $\vec{v}_2$ now form an orthogonal basis with $\vec{v}_1$ indicating the principal direction of scattering. The variance in each direction is given by the eigenvalues λ_1 and λ_2. In this respect, the anisotropy of the scattering can conveniently be

Biomedical Optics EXPRESS

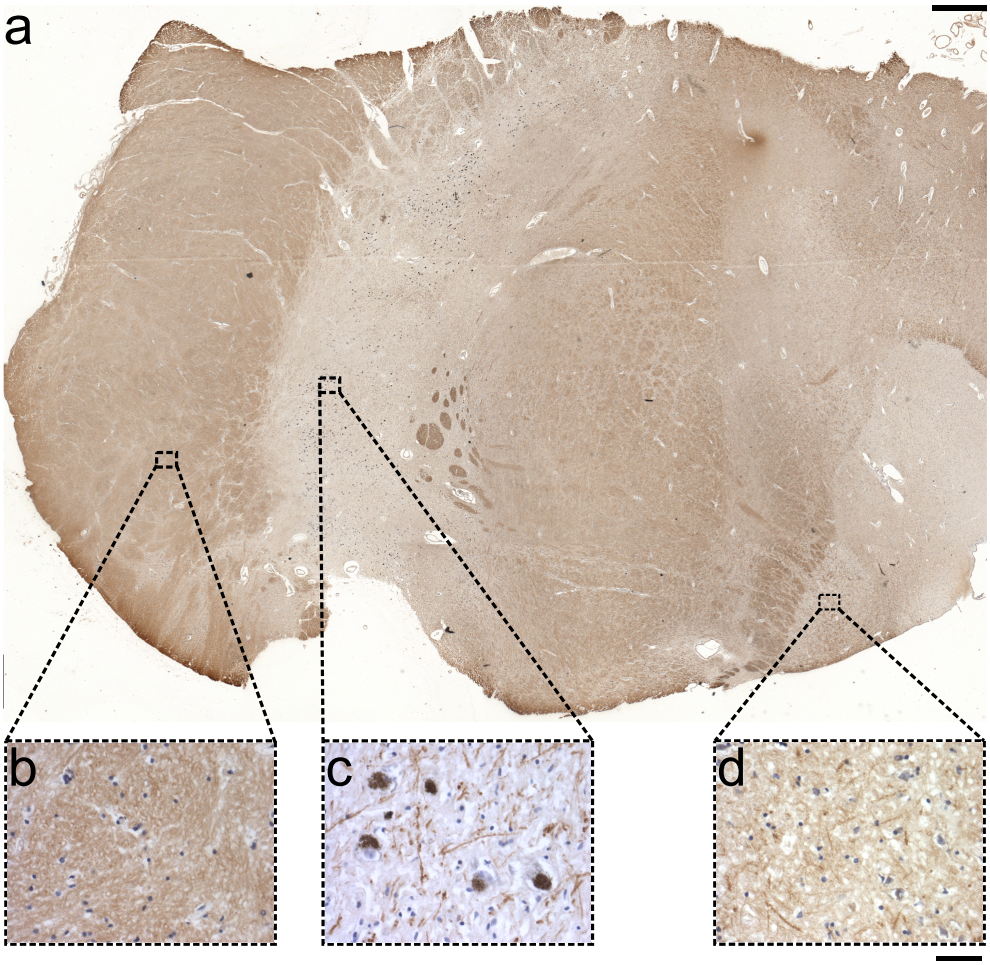

Fig. 4. (a) Overview of an IHC staining of MBP from tissue of the CTR sample in a neighboring section of those that have been investigated using x-rays. The staining is resulting in a brown color due to the product of the reaction between horseradish peroxidase and DAB. The intensity of the color is dependent on the amount on MPB present in the region, Scale bar: 500 µm (b-d) Close-up regions show the myelin content of (b) Crus cerebri, (c) Substantia Nigra, and (d) Red Nucleus. Scale bar: 50 µm.

quantified by the unitless parameter ω defined as

$$\omega = \frac{|\lambda_1 - \lambda_2|}{\lambda_1 + \lambda_2} .$$

Note that prior to the PCA analysis, one typically has to define a range of q-vectors, here an annulus of the diffraction pattern, of which the anisotropy is computed [30]. We found that indeed, the anisotropy in the Crus Cerebri region is high and an orientation can be clearly deduced from the diffraction, as visualized in Fig. 5. The orientation in Fig. 5(b) is coded in color as well as by arrows indicating the nerve fiber orientation (orthogonal to the direction of $\vec{v}_1$) in the Crus Cerebri. The anisotropy of the diffraction reported here is based on the diffraction from the second order of the myelin signal, as shown in Fig. 6(b), which is more anisotropic in contrast to the third order (see e.g. Fig. 6(b)). In a similar fashion, we have computed the orientation and anisotropy of the third order of the myelin signal (data not shown), which showed that the

Biomedical Optics EXPRESS

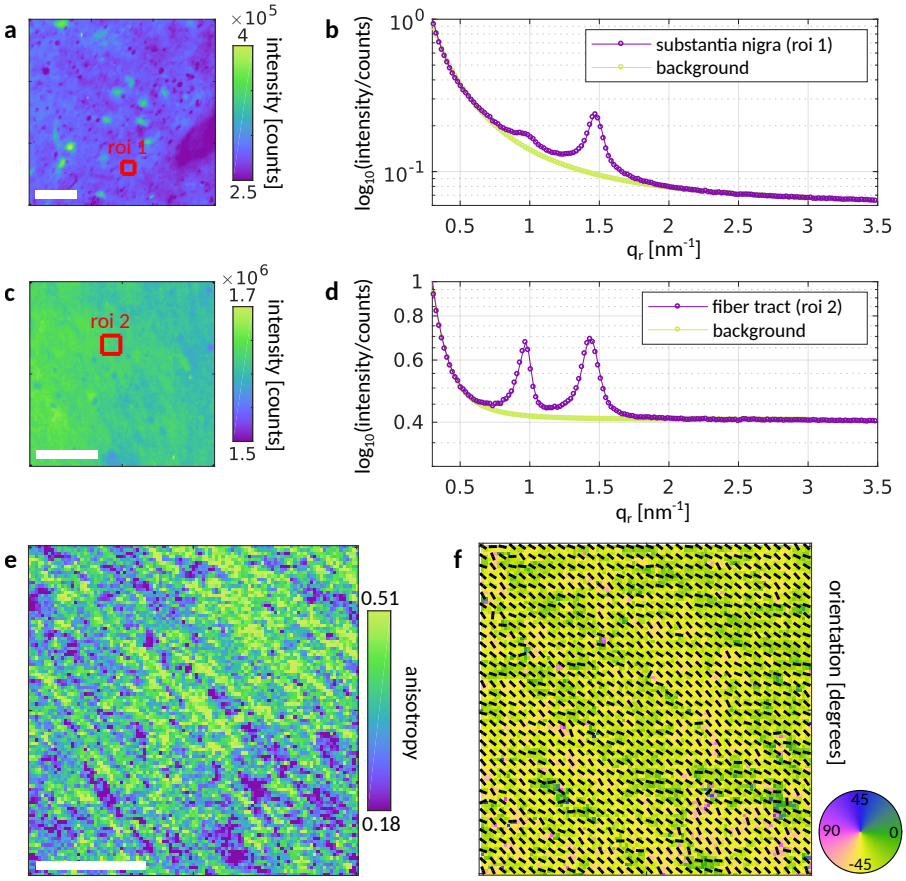

Fig. 5. (a-d) Structure factor analysis of the SAXS signal. (a) Darkfield map of SN tissue from CTR sample. Data from region 1, marked in red, was averaged and azimuthally integrated, as shown in (b). (c) Darkfield map of FT tissue from CTR sample. Again, data from region 2, marked in red, was averaged and azimuthally integrated, as shown in (d). (e-f) Principal component analysis of fiber tract tissue of the Crus Cerebri. (e) Anisotropy of the myelin diffraction. (f) Orientation of the long axis of the myelin sheath. Orientation of the axons is both color coded and indicated by superimposed black lines. Scale bar 100 μm.

orientation of the second and third order of the myelin signal are clearly correlated, with the anisotropy of the third order being far less pronounced.

In addition to the anisotropy and orientation reported above, further structural quantities can be extracted from the myelin signal, in particular lamellar repeat spacing and peak width. The spatial fine structure of this signal could be of interest for future studies addressing in particular the lamellar structure of myelin and related pathologies. In this work, however, we want to draw the attention to a particularly surprising finding: apart from the predominant lamellar signal of the myelin sheath, we also found isolated spots in the tissues of both PD and CTR, where the diffraction pattern exhibited a hexagonal symmetry. This is exemplified in Fig. 6, where next to a typical lamellar pattern we also present a diffraction pattern with hexagonal symmetry, along with the associated locations in the darkfield map (indicated by arrows). From the fact that higher order reflections are not visible in the diffraction signal, we infer that the underlying lipid arrangement is rather hexatic than strictly hexagonal, i.e. exhibits directional but no positional long range order. To our knowledge, such a phase behavior of the myelin sheath has so far only

Biomedical Optics EXPRESS

been observed in *in vitro* model systems mimicking the chemical composition of the myelin sheath [31] but has not been observed previously *in situ* in studies employing human tissue, even though an hexagonal phase was already proposed as early as [32]. To further quantify the hexagonal scattering, we have averaged all patterns exhibiting clear hexagonal symmetry as well as patterns in the bulk of the tissue. For both averaged patterns, we have performed an azimuthal integration to once again determine the peak positions and peak widths. Again, we find that in the bulk, the ratio of the lamellar positions of the second and third reflection order is given by the ratio 3/2. The reflections of the hexatic phase are found at $q_r^{(\mathrm{hex})} = 1.43\,\mathrm{nm}^{-1}$ corresponding to a period of $a_H = \frac{4\pi}{\sqrt{3}q_r^{(\mathrm{hex})}} = 5.1\,\mathrm{nm}$ which is well on the order of the thickness of a single bilayer. The peak positions and peak widths are summarized in Tab. 1.

In summary, we hypothesize that the myelin sheath, which would normally be a lamellar stack of lipid membranes surrounding the axon of the neuron as sketched in Fig. 6(d) forms an inverse hexatic phase, as shown on the right. Clearly, the presence of an hexatic phase could result from the rather invasive sample preparation. The effect of temperature, freezing and drying has been extensively studied in the literature , see e.g. [29, 32–35] and references therein, however, the values reported in the references cannot be directly compared to the values reported here, primarily because the extracted nerve was typically re-immersed in a buffer solution after freezing or heating. Therefore, future extension of this work has to investigate whether myelin is indeed capable of forming hexatic phases.

Table 1. Summary of peak positions and peak widths as determined from the respective structure factors shown in Fig. 5 and Fig. 6.

	$q_r^{(2,0)}\,[\mathrm{nm}^{-1}]$	$q_r^{(3,0)}\,[\mathrm{nm}^{-1}]$	$\sigma^{(2,0)}\,[\mathrm{nm}^{-1}]$	$\sigma^{(3,0)}\,[\mathrm{nm}^{-1}]$	$q_r^{(3,0)}/q_r^{(2,0)}$
ROI 1	0.98	1.47	0.09	0.09	1.50
ROI 2	0.96	1.44	0.08	0.10	1.50
ROI 3	0.93	1.39	0.09	0.08	1.49
Hexatic phase	$q_r^{(\mathrm{hex})}\,[\mathrm{nm}^{-1}]$	1.43	$\sigma^{(\mathrm{hex})}\,[\mathrm{nm}^{-1}]$	0.06	

While myelin is an abundant component of neuronal tissue, by accessing the wide-angle scattering range, smaller crystalline components can be localized by scanning micro-diffraction. Indeed, pronounced wide-angle reflections from crystalline domains where observed in the present samples. In the following, we aimed at localizing these crystalline domains and determining their origin (Fig. 7). Localization was achieved in three steps: First, background was subtracted from each diffraction pattern. Secondly, crystalline reflections were identified in each diffraction pattern by applying a threshold of 10 counts (Fig. 7(b)). Thirdly, intensity of the reflections above $1.6\,\mathrm{nm}^{-1}$ and localized in the previous step was integrated. Intriguingly, following this procedure, we noticed that the PD patient sample contained approximately ten times more crystallites than the CTR patient sample (Fig. 7(d)).

To determine the origin of such diffraction, we have estimated the unit cell parameters from diffraction patterns originating from single crystalline domains. The unit cell parameters were referenced against the Cambridge Structural Database (CSD). Anhydrous cholesterol appeared the closest match to the given unit cell parameters. To verify that cholesterol had indeed crystallized primarily in the PD sample, we performed a maximum projection of a data set containing larger amounts of crystallites. In a maximum projection of a stack of 2D diffraction patterns, the maximum value was calculated for each pixel along the stacking dimension, to accumulate all reflections in the acquired data onto a single 2D diffraction pattern. In a second

Biomedical Optics EXPRESS

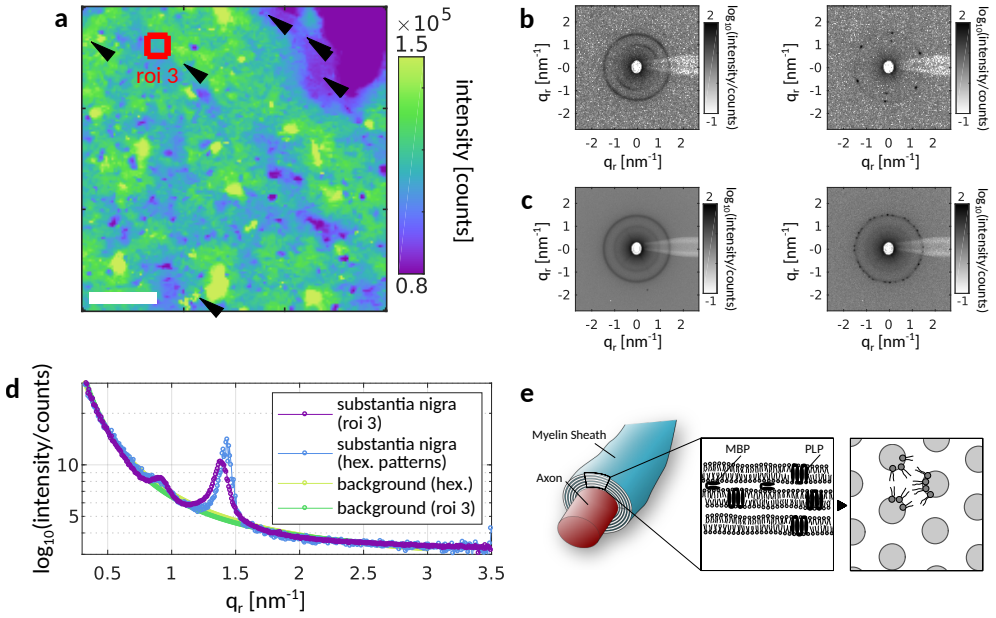

Fig. 6. (a) X-ray raster scan (darkfield contrast) of a brain tissue section (SN region) from a Parkinson's disease patient. Arrows indicate locations at which an hexatic lipid phase could be identified. Scale bar: 100 µm (b, left) Myelin signal as can be observed throughout the scanned sample region, while (b, right) a signal resembling an hexatic lipid bilayer phase can only be found at isolated locations in the sample, as marked by arrows in (a). (c, left) Averaged signal from roi 3 as marked in red in (a). (c, right) Averaged signal from locations where an hexatic phase was identified. (d) Both patterns in (c) have been angular averaged to identify the peak locations and peak widths. (e) Sketch of the myelin sheath surrounding the axon of a nerve cell. A zoom region shows a sketch of the lamellar stacking of lipid bilayers in the myelin sheath with myelin basic protein (MBP) and proteolipid protein (PLP) as major protein constituents of the myelin sheath. Based on the data it can be speculated that the myelin sheath can undergo a phase transition into an inverse hexagonal phase, as shown on the right. MBP: Myelin basic protein, PLP: Myelin proteolipid protein. Subfigure (e) with adaptions from [36].

step, the maximum projection was angular averaged to give a one-dimensional representation taking into account all reflections occurring within the scan (blue curve in Fig. 7(e)). Finally, reflection positions (red lines in Fig. 7(e)) were simulated using the values reported in [37] for the unit cell of anhydrous cholesterol and superimposed onto the one-dimensional (powder averaged) data. Data and simulation agree well up to approximately 6 nm^{-1} where the degeneracy of the triclinic lattice spacing d_{hkl} is low, hence making it highly plausible that the crystallites were indeed formed by anhydrous cholesterol. Subsequently, we correlated the spatial distribution of cholesterol crystals with a 2D raster image (darkfield contrast, Fig. 8(a)), and optical micrographs (Fig. 8(b)), as well as 2D maps of the x-ray fluorescence signal, namely the summed fluorescence intensity (Fig. 8(d)) and the Zn, Fe and Cu fluorescence maps (Fig. 8(d-f)). It can be observed that cholesterol crystals do not co-localize with the distribution of SN neurons and that the cholesterol crystals appear in all cases to be mostly situated in the extracellular space.

Histological results: The tissue blocks were embedded in paraffin and the tissue sections were stained with hematoxylin-eosin for a morphological evaluation and also with two different antibodies: anti-aSyn and anti-p129-aSyn. In the PD sample, HE-stain showed the presence of intracellular aggregates that were identified as Lewy bodies (LB, Fig. 9, top) and no other kinds

Biomedical Optics EXPRESS

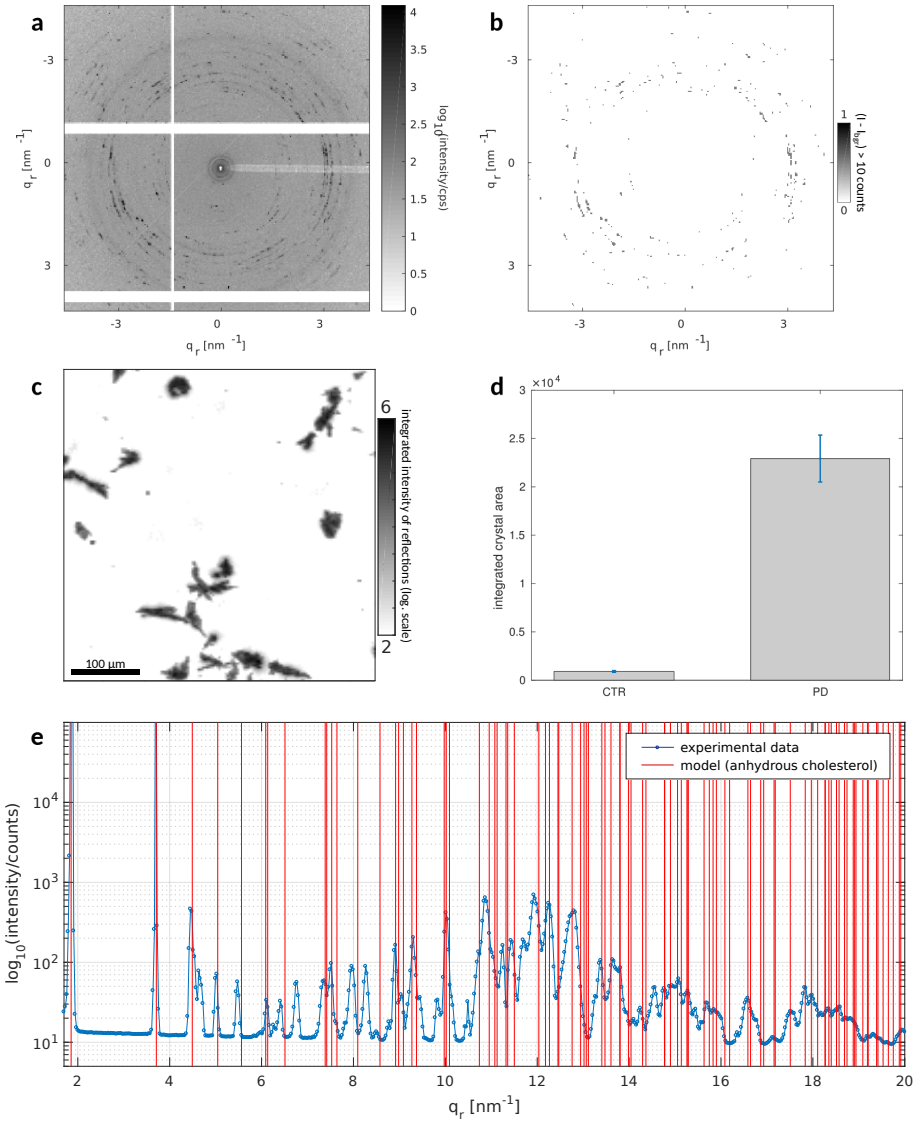

Fig. 7. Crystalline reflections from anhydrous cholesterol. (a,b,c) Illustration of the crystal localization procedure. (a) Diffraction pattern showing the presence of crystalline diffraction peaks in the wide-angle region. (b) Thresholded diffraction pattern (background subtracted) for a threshold of 10 counts. (c) Summing the intensity of the reflections identified by the logical masking procedure in (b) for each scan points yields a map of the crystalline domains of the sample. (d) Summed number of scan points exhibiting crystalline reflections within the CTR and PD sample. (e) Azimuthal integration of the maximum projection of the scan (blue lines and dots) with red lines superimposed corresponding to reflections that would result from anhydrous cholesterol.

of aggregates were found. On the other hand, the CTR sample was negative for aggregates. The LB found were mostly present in the intracellular space and their diameter was ranging from 2 to 15 µm.

To confirm that the intracytoplasmic inclusions that resembled LB contained aSyn, the sections were stained with antibodies against aSyn and its phosphorylated form, which is mostly found in

Biomedical Optics EXPRESS

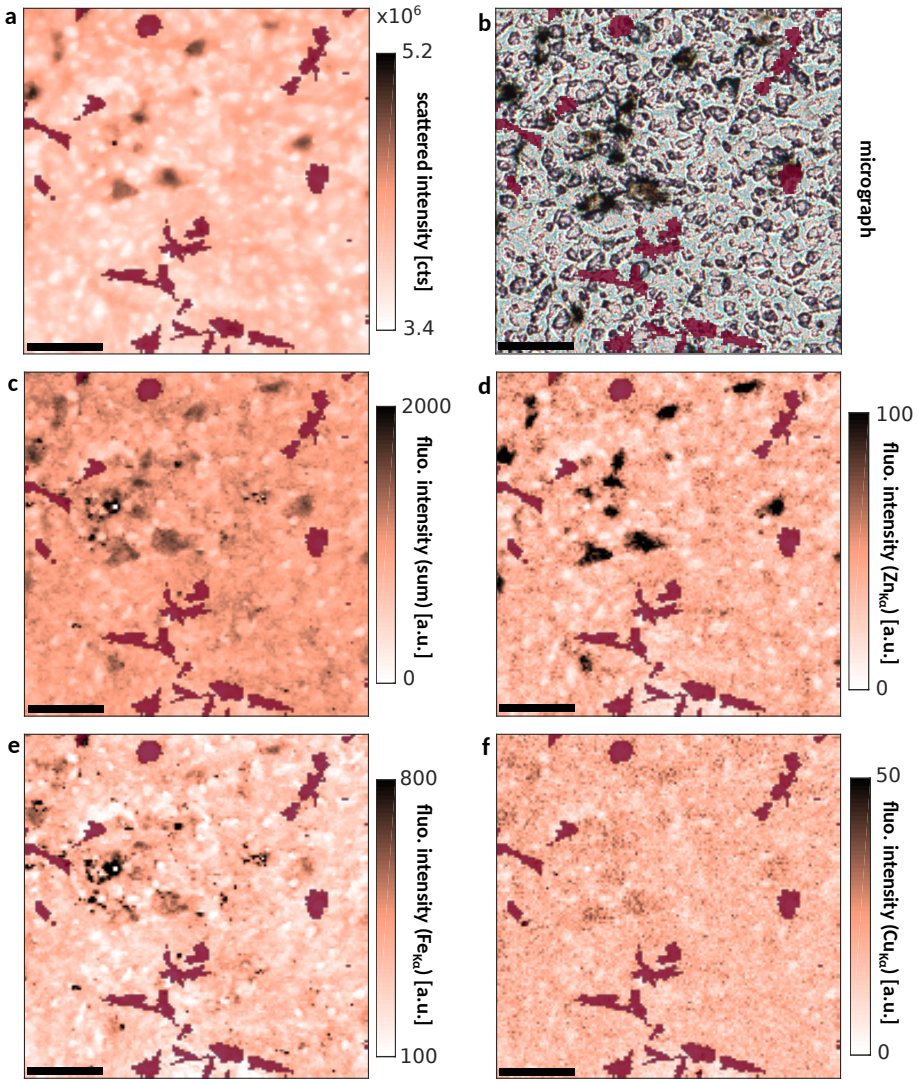

Fig. 8. Semitransparent map of the distribution of crystalline aggregates (red areas) overlaying (a) the STXM map (darkfield contrast), (b) optical micrograph, (c) total fluorescence intensity, (d) Zn Kα fluorescence map, (e) Fe Kα fluorescence map and (f) Cu Kα fluorescence map. Scale bar: 100 μm.

LB. Both antibodies confirmed the presence of LB solely in the PD sample.

4. Discussion and outlook

In our experiment, we have combined scanning X-ray fluorescence and X-ray diffraction to map neuronal tissues with high spatial resolution. We chose SN of a PD patient as well as a control, aiming at a translation of advanced structural techniques to biomedical research in PD, and more generally in neurodegeneration.

We found that the scanned PD tissue displayed a well-documented metal dys-homeostatsis [5, 38]. Our data are in agreement with previous studies, which showed that the highest amount of metals on the human SN are contained inside the neurons while in the extracellular space

Biomedical Optics EXPRESS

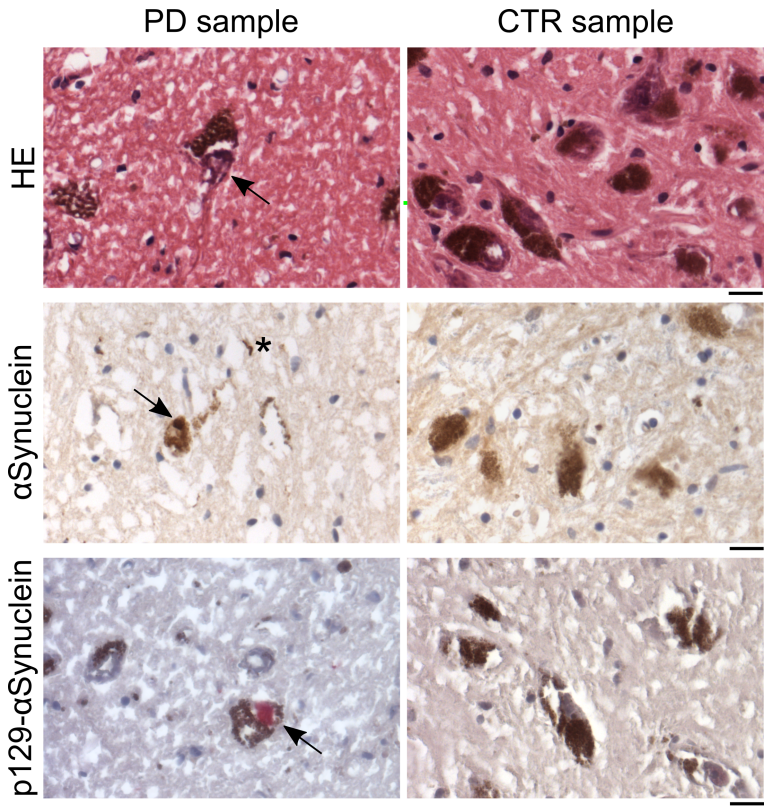

Fig. 9. Histological evaluations of the samples. Each row represents the primary antibody used, both for PD (left column) and CTR (right column) column. The arrows point to Lewy bodies and the star highlights a Lewy neurite. Scale bar: 20 μm.

lower concentrations are reported [5, 39]. The entire elemental spectra of all scans were analyzed to identify a signal suitable to discriminate between intracellular and extracellular space. The neurons analyzed in SN are mostly NM positive cells, and previous reports pointed out that NM is rich in Fe, Cu and Zn [40]. Among these elements, Zn was the element that displayed the greatest concentration difference between intra- and extracellular content. Therefore, a threshold on the Zn signal was chosen for automated identification of the two regions in the form of a logical mask. Using these masks for all scans, four different spectra were computed: intracellular and extracellular (sum) spectrum for PD, as well as intracellular and extracellular (sum) spectrum for the CTR sample.

Compared to the CTR, Fe amounts were found to be three times higher in the extracellular space for the PD tissue. This is consistent with results from other groups [41]. Intriguingly, the Fe distribution in the extracellular space does not seem to follow a regular pattern. Indeed, bright spots of Fe appear frequently in scans. The reason for the presence of these irregular Fe deposits deserves further investigation. The methods followed in sample preparation (like the special cryomatrix used, the temperature for sectioning and the special Teflon-coated blades) should have prevented the displacement of metal between the inside and outside of the cell. The extracellular Fe depositions might thus indicate some still unexplored mechanism in the pathology. Cu concentration in the PD patient, on the other hand, are reduced by about 50% in both the intracellular and extracellular space. This is in line with a recent report [38]. The analysis of metal content in tissue is further motivated by the fact that *in vitro* experiments indicate that

Biomedical Optics EXPRESS

the interaction of aSyn with several metals (like Fe and Cu) promotes its aggregation [42–44].

Hematoxylin-eosin staining is routinely performed in the course of histological evaluations as it provides a morphological characterization of the tissue [26]. In the PD sample analyzed we could detect LBs by HE staining as they appeared with a dense eosinophilic core surrounded by a clearer halo. The stain with aSyn and p129-aSyn confirmed the presence of LBs and of Lewy neurites. All in all, the results are in line with 'classic' PD histology, while the control sample was devoid of these features. Even though LBs were identified by histological staining of adjacent sections, we were unable to locate LBs during the scanning diffraction experiment, which is a challenging task given their low number and small size ranging between 2 and 6 μm [3]. It would be an important future goal to elucidate the molecular structure of the LB by x-ray micro-diffraction, using the scanning approach presented here. A similar approach using tissue from Alzheimer's diseased patients has already proven successful in providing useful insights on the development of amyloid plaques [45].

Contrarily, we found a pronounced diffraction signal corresponding to highly ordered crystalline structures which formed extended domains, primarily in the PD sample, and could show that the crystallites are formed by cholesterol. The formation of cholesterol crystals could have been caused by the fact that the tissue was left to dry at 60°C, which might have triggered a phase transition, typically occurring during cooling of the sample at around 44°C [46]. However, cholesterol crystals also seem to occur in preparations of nervous tissue where the sample was dried at temperatures lower than 44°C [39]. The fact that crystallization took primarily place in the PD sample could be explained in at least two ways. One is that the amount of cholesterol in the PD sample was higher than the control. A lipidomic study is in support of this (first) hypothesis. In fact, it has been reported that in the visual cortex of PD patients there is an increased cholesterol level compared to control patients [47]. The other explanation is that the proportion of the different phospholipids and cholesterol in the membrane was different between the patient and control. This could lead to a lowering of the phase transition temperature thus facilitating the phase change of cholesterol with consequent cholesterol crystal formation. This hypothesis is also supported by a study in which the author could correlate the variation of phospholipid composition in the membrane to its damage in PD patients [48].

Either way, cholesterol and several oxysterols have been correlated with their role in aging and in neurodegenerative pathologies such as Alzheimer disease [49]. The blood brain barrier naturally occurring in the brain prevents cholesterol and its derivatives to enter the brain from the blood stream. Astrocytes produce most of the cholesterol in the brain. Variations of cholesterol content are related to metabolic dysfunctions in the pathway connected to this lipid [11]. Animal studies in mice correlate a diet rich in fat or cholesterol with the worsening of neurotoxins-induced loss of dopaminergic neurons [50]. In *in vitro* studies, aggregated forms of aSyn could disrupt phospholipidic bilayers that where rich in cholesterol [51].

Regarding cholesterol in PD, one should also keep in mind the role of oxysterols. These are oxidized forms of cholesterol. They have exactly the same structure of cholesterol with the addition of one (or more) hydroxyl groups on the sterol nucleus or on the side chain. They are chemically very similar to their cognate and they arise from the ROS produced in the cells that are particularly abundant in neurodegenerative diseases such as PD. These molecules have been found to be in excess in PD patients and they are also suggested to be involved in the etiopathology of PD [11].

Besides having identified and localized cholesterol as tissue component, XRD scanning of the tissue also revealed a pronounced anisotropic SAXS signal, which can be attributed to myelin. The orientation and the peak spacings of the myelin sheath can thereby be mapped throughout the tissue, quantifying the underlying axonal orientation. Interestingly, it was found that in sparse locations through the sample, the myelin scattering suddenly became hexagonal with no long-range correlation, pointing at a hexatic phase of myelin at these spots. Future work will

Biomedical Optics EXPRESS

have to corroborate this finding and verify whether it is intrinsic or results from an invasive sample preparation.

In conclusion, in our study we have combined standard histological techniques with advanced spatially resolved XRD and XRF. A pronounced difference was found in trace metal composition of the PD sample compared to the control. In addition, a crystalline diffraction signal attributed to cholesterol was observed to be more abundant in the PD tissue. Given the exiguity of patients, the biological findings need to be further characterized in a larger cohort. Overall, the approach described here for the characterization of human tissue is new and promising for future applications such as the discovery of new biomarkers for neurodegenerative diseases.

Funding

Deutsche Forschungsgemeinschaft (DFG) (EXC 171, SFB 937).

Acknowledgments

The authors thank Elisabeth Barski for expert technical assistance and Manfred Burghammer for excellent working conditions at beamline ID13.

Disclosures

The authors declare that there are no conflicts of interest related to this article.